



Corrosion behavior of dual-main-phased $(\text{Nd}_{0.8}\text{Ce}_{0.2})_2\text{Fe}_{14}\text{B}$ magnets with and without annealing process

Xiao-Ning Shi, Ming-Gang Zhu* , Rui Han, Li-Wei Song, Wei Li

Received: 30 September 2016/Revised: 10 January 2017/Accepted: 7 September 2017/Published online: 21 November 2017
© The Nonferrous Metals Society of China and Springer-Verlag GmbH Germany 2017

Abstract In this work, the corrosion behavior of the sintered $\text{Nd}_2\text{Fe}_{14}\text{B}$ in which Nd was substituted by Ce to form dual-main-phased magnet with/without annealing process was studied. The mass loss of as-sintered magnets (SM) is larger than that of as-annealed magnets (AM) in the accelerated corrosion tests. In particular, the mass loss of SM increases sharply when the corrosion time increases to 48 h. The free corrosion current of the SM samples is larger than that of AM in $0.1 \text{ mol}\cdot\text{L}^{-1}$ HCl; this is due to that the content of RE-rich phase at the intergranular triple junctions (TJs) of the SM samples is larger than that of AM samples and the corrosion rate of the RE-rich phase at the TJs is higher than that at grain boundaries. But the free corrosion current of the SM samples is smaller than that of AM samples in 3.5 wt% NaCl as the electron transfer resistance (R_{ct}) of SM is larger than that of AM. Inductive loop in the Nyquist diagrams at low frequency of SM is observed, which originated from the pitting. It shows that pitting of SM occurs more easily than that of AM. Corrosion morphology of samples indicates that the corrosion area of SM is bigger and deeper than that of AM after accelerated corrosion for 60 h. Through the annealing process, the distribution of rare-earth-rich phase becomes more uniform, which changes the free corrosion current and effectively suppresses the occurrence and propagation of pitting.

Keywords NdFeB magnet; Annealing process; Intergranular corrosion; Pitting corrosion

1 Introduction

Sintered magnets are widely used because of the excellent magnetic properties [1, 2]. It is reported that the highest magnetic energy product of the magnets has been reached as high as $4.7 \times 10^5 \text{ J}\cdot\text{m}^{-3}$ [3]. In order to meet different application requirements, different elements are added to the magnets. The heavy rare earth (HRE) elements, such as dysprosium (Dy) and terbium (Tb), are added to $\text{Nd}_2\text{Fe}_{14}\text{B}$ magnets for elevating the coercivity (H_{cj}) of and reducing the temperature coefficient of magnets as $(\text{Dy/Tb})_2\text{Fe}_{14}\text{B}$ has higher magnetic anisotropy field than $\text{Nd}_2\text{Fe}_{14}\text{B}$ [4–7]. Light rare earth element Ce is abundant in nature, especially in China. Much effort has been made in substitution of Nd for Ce to avoid overuse of rare earth Nd [8–10].

The microstructure of sintered Nd–Fe–B magnet presents ferromagnetic matrix phase ($\text{Nd}_2\text{Fe}_{14}\text{B}$) which is surrounded by Nd-rich intergranular phase [11, 12], and the magnet is highly susceptible to corrosion because of the high reactivity of Nd and the galvanic coupling between Nd-rich phase and $\text{Nd}_2\text{Fe}_{14}\text{B}$ phase [13–15].

An optimized heat treatment allowed the creation of an extremely uniform RE-rich film in the grain boundary interfaces (GBs) and made it possible to reach a high coercivity [16]. Moreover, the action makes the small-sized (Pr, Nd)-rich phase grains harmoniously distribute at the intergranular triple junctions (TJs) [17]. The corrosion rate of RE-rich phase at the TJs is higher than that at GBs [17, 18]. From the perspective of the distribution with RE-rich phase, the act of the annealing process improves the corrosion resistance of the magnet. But the fine grid structure with $\text{Nd}_2\text{Fe}_{14}\text{B}$ and Nd-rich phase reduces the corrosion resistance of magnets by heat treatment [19]. So

X.-N. Shi, M.-G. Zhu*, R. Han, L.-W. Song, W. Li
Division of Functional Material, Central Iron & Steel Research Institute, Beijing 100081, China
e-mail: mgzhu@sina.com

it is dubious as to how the annealed process can influence corrosion resistance.

For the dual-main-phased $(\text{Nd}_x\text{Ce}_y)_2\text{Fe}_{14}\text{B}$ magnet, the cerium element is more easily distributed at the triple-point junctions than at neodymium [20]. The RE-rich phase has a lower melting point than the Nd-rich phase, meaning that RE-rich phase has a better liquidity than Nd-rich phase. Therefore, the distribution of intergranular phase can be significantly affected by annealing process.

The corrosion of the dual-main-phased $(\text{Nd}_x\text{Ce}_y)_2\text{Fe}_{14}\text{B}$ has already been studied [21]. However, the influence of annealing process on corrosion has rarely been reported to our best knowledge. The present work studies the corrosion resistance of as-sintered magnets (SM) and as-annealed magnets (AM) of $(\text{Nd}_{0.8}\text{Ce}_{0.2})_2\text{Fe}_{14}\text{B}$ magnets referred to as Ce20. The mass loss was measured in accelerated corrosion tests. The electrochemical character was researched in $0.1 \text{ mol}\cdot\text{L}^{-1}$ HCl and 3.5 wt% NaCl.

2 Experimental

Ce20 magnets were prepared by conventional dual-main-phased magnet preparation methods. The temperature of sintered magnet was determined at $1000 \text{ }^\circ\text{C}$, and the secondary annealing temperature was defined at $450 \text{ }^\circ\text{C}$ without first annealing treatment.

The dimensions of the magnet specimens used for accelerated corrosion tests were $\Phi 10 \text{ mm} \times 10 \text{ mm}$. Accelerated corrosion tests were performed under conditions of $120 \text{ }^\circ\text{C}$ and 100% relative humidity for 12, 24, 36, 48 and 60 h, respectively. The corrosion products were removed according to the standard of GB/T24195-2009. The magnetic properties of the samples before and after corrosion were analyzed by a hysteresis loop instrument (NIM-2000, National Institute of Metrology, China). The back-scattered electron (BSE) images were captured by Phenom ProX. Content of the triple junction was estimated by the ratio of the RE-rich phase (white contrast) area (A_1) to the whole area (A_0) in the typical back-scattered images of the magnet using the Digimizer software. The potentiodynamic polarization curves were tested by electrochemical analyzer (CHI660D). The electrochemical impedance spectra (EIS) tests were performed by Gamry Co. interface 1000. The amplitude of the sinusoidal perturbation applied to the electrode was 10 mV. All electrochemical specimens were kept in 3.5 wt% NaCl solution for 0.5 h to stabilize the stationary potential of the specimens. The electrochemical measurements were taken by a conventional three-electrode electrochemical cell with a saturated calomel electrode (SCE) as the reference, a Pt foil as the auxiliary electrode and the samples Ce20 as the working electrode.

3 Results and discussion

BSE images of SM and AM samples are shown in Fig. 1. The dark regions refer to the main phases, and the light regions represent the intergranular phases. For SM samples, the content of TJs is $\sim 9.2 \text{ vol}\%$. But for AM samples, the content % of TJs decreases to $\sim 5.6 \text{ vol}\%$. Obviously, the annealing process significantly changes the distribution of RE-rich phase.

Figure 2 shows the results of accelerated corrosion tests under conditions of $120 \text{ }^\circ\text{C}$ and relative humidity of 100%. The results show that the mass loss increases with increasing corrosion time. However, the mass loss of SM samples increases sharply when the corrosion time increases to 48 h. The rate of mass loss for AM samples is the highest in the first 12 h and then gradually reduces with further corrosion. The mass loss rate of SM sample has two inflection points at 12 and 48 h. Compared to that of AM samples, mass loss of SM samples is larger, which means that intergranular phases of SM samples are more likely to dissolve in the initial 12 h. The inflection point of 48 h for SM samples shows that SM samples crack more severe than AM samples. It is reported that pits start at Nd-rich phase and then propagate along GBs, and the combination of grain boundary failure, pitting and hydrogenation leads to a degradation of Nd-Fe-B magnets under conditions of $85 \text{ }^\circ\text{C}$ and relative humidity of 80% [22]. The differences in the degradation of the two samples ought to be associated with pitting and the propagation of pitting.

Figure 3a demonstrates potentiodynamic polarization curves of SM and AM Ce20 in $0.1 \text{ mol}\cdot\text{L}^{-1}$ HCl aqueous solutions. The corrosion potential (E_{corr}) and corrosion current density (i_{corr}) are listed in Table 1 calculated by Tafel linear extrapolation method. The E_{corr} of AM samples is more positive compared to that of SM samples. The i_{corr} of SM samples is larger than that of AM samples. As anode, RE-rich phase loses electrons. From the E -pH diagram [23], the RE displays RE^{3+} when it loses electron, it can be got that the reflections $\text{Ce} \rightarrow \text{Ce}^{3+} + 3\text{e}^-$, $\text{Nd} \rightarrow \text{Nd}^{3+} + 3\text{e}^-$ and $\text{Fe} \rightarrow \text{Fe}^{2+} + 2\text{e}^-$ and the main phases $\text{Nd}_2\text{Fe}_{14}\text{B}$ and $\text{Ce}_2\text{Fe}_{14}\text{B}$ gains electrons as cathode and the reaction is $\text{H}^+ + \text{e}^- \rightarrow \text{H}$ [24]. Shedding particles can be seen clearly in the test process.

The corrosion mechanism of Nd-Fe-B magnets in HCl solution is mainly selectively intergranular corrosion [25], and the particles fall off [26]. From BSE images, it can be seen that the TJs content of SM samples is larger than that of AM samples. And the corrosion rate at TJs is higher than that at GBs [18]. So, the corrosion current of SM samples is larger than that of AM samples.

Figure 3b shows potentiodynamic polarization curves of SM and AM samples in 3.5 wt% NaCl aqueous solutions. Table 1 shows that the free corrosion voltage (E_{corr}) of SM and AM samples is -0.7786 and -0.7818 V , respectively,

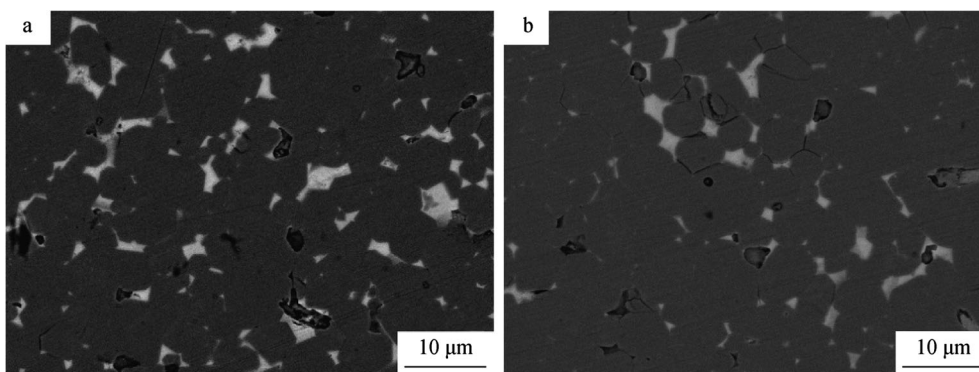


Fig. 1 BSE images of dual-main-phased **a** SM and **b** AM (Nd_{0.8}Ce_{0.2})₂Fe₁₄B

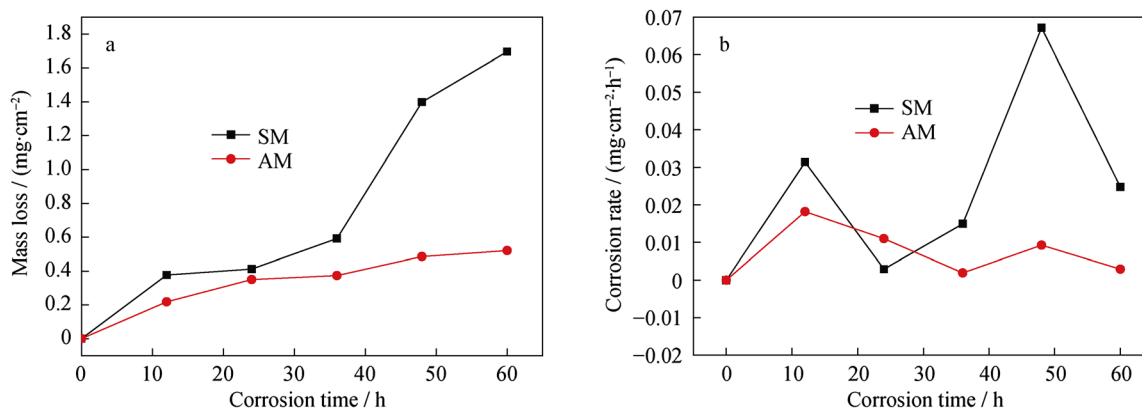


Fig. 2 **a** Mass loss and **b** corrosion rate of SM and AM samples with time at 120 °C in 100% relative humid atmosphere

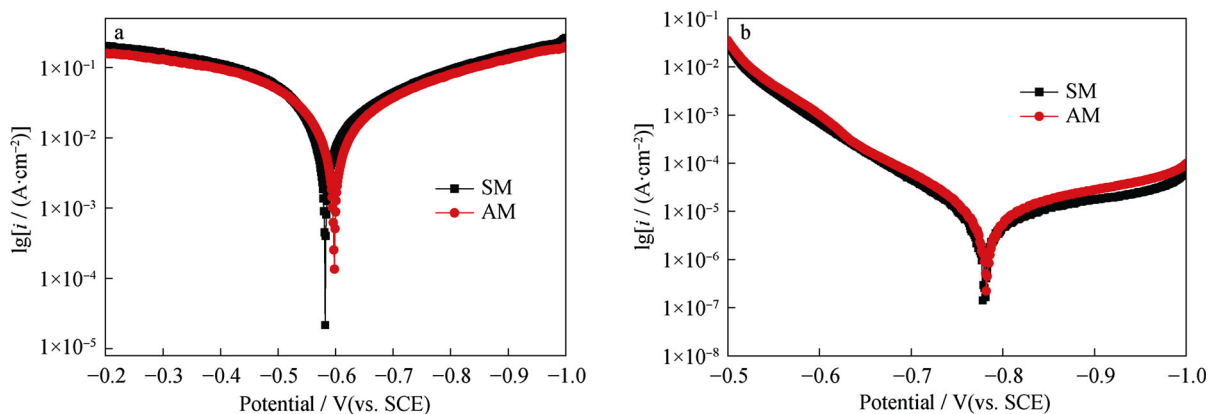


Fig. 3 Typical potentiodynamic polarization curves of SM and AM samples in **a** 0.1 mol·L⁻¹ HCl and **b** 3.5 wt% NaCl

Table 1 Electrochemical parameters of SM and AM in 0.1 mol·L⁻¹ HCl aqueous solutions and 3.5 wt% NaCl aqueous solutions

Samples	HCl aqueous solutions		NaCl aqueous solutions	
	E_{corr}/V	$i_{\text{corr}}/(A\cdot\text{cm}^{-2})$	E_{corr}/V	$i_{\text{corr}}/(A\cdot\text{cm}^{-2})$
SM	-0.583	2.359×10^{-2}	-0.7786	8.282×10^{-6}
AM	-0.603	1.759×10^{-2}	-0.7818	1.179×10^{-5}

and the moving direction of corrosion potential is similar to the results in 0.1 mol·L⁻¹ HCl. The free corrosion current (i_{corr}) of SM and AM samples is 8.282×10^{-6} and 1.179×10^{-5} A·cm⁻², respectively. The free corrosion current of SM samples is smaller than that of AM samples, which is opposite in HCl aqueous solution. The anode loses electron, and the reactions is $\text{Nd} \rightarrow \text{Nd}^{3+} + 3\text{e}^-$, $\text{Ce} \rightarrow \text{Ce}^{3+} + 3\text{e}^-$ and $\text{Fe} \rightarrow \text{Fe}^{2+} + 2\text{e}^-$. The main course of Nd₂Fe₁₄B and Ce₂Fe₁₄B as cathode is the reaction of

$O_2 + 2H_2O + 4e^- \rightarrow 4OH^-$ [27] in NaCl aqueous solution. The cations Nd^{3+} , Ce^{3+} and Fe^{2+} combine with OH^- to form passive film [28].

Applying a small alternating current (AC) signal and measuring the response of the electrochemical system can be used to study the corrosion of metals [29]. The EIS tests of the samples were not conducted in HCl solution, because the disturbance of open-circuit voltage is greater than 10 mV which is comparative to voltage amplitude.

Figure 4 displays the Nyquist diagrams of EIS for SM and AM samples in 3.5 wt% NaCl. The Nyquist diagrams show the imaginary impedance values (Z'') plotted against the real impedance (Z') values obtained at each polarization frequency. The radius of SM samples is larger than that of AM samples, meaning that SM samples perform a greater transfer resistance. Inductive loop at low frequency of SM samples is observed which originated from the pitting corrosion on the working electrode as a result of the adsorptions of Cl^- .

To fit the EIS results accurately, constant phase angle element (CPE, designated as Q) was used instead of the pure capacitance. The admittance of CPE (Y_Q) can be expressed by the following equation:

$$Y_Q = Y_0(j\omega)^n \quad (1)$$

where j is the imaginary number, ω is the angular frequency, and Y_0 and n are defined as the admittance constant and the empirical exponent of the CPE respectively. Inductive loop is equivalent to inductance (L) and inductive reactance (R_L) which represent pitting corrosion. The equivalent circuit is shown in Fig. 5. In this circuit, R_s is the electrolyte resistance between the working electrode and the reference electrode, and R_{ct} is the transfer resistance of electrons of double electrode layer. The data fitted by Gamry's software are listed in Table 2. The value of L is relevant to the thickness of the passivation film [30]. From the fitting parameters of EIS, the electron transfer resistance (R_{ct}) of AM samples is lower than that of SM

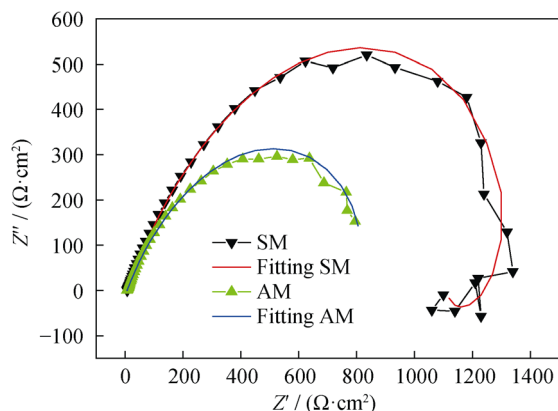


Fig. 4 Nyquist diagrams for SM and AM samples in 3.5 wt% NaCl

Table 2 Fitting parameters of Nyquist diagrams

Samples	R_s/Ω	R_{ct}/Ω	$Y_0/$ ($10^{-6}F \cdot cm^{-2}$)	n	L/H	R_L/Ω
SM	6.220	998.9	659.7	0.6847	1460.0	746.4
AM	6.957	895.1	443.5	0.6856	–	–

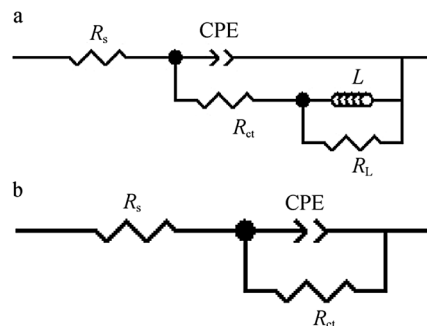


Fig. 5 Equivalent circuit for EIS data of **a** SM and **b** AM samples

samples in 3.5 wt% NaCl. So, the annealed process reduces the electron transfer resistance (R_{ct}).

The magnetic properties of the corrosion samples were analyzed by NIM-2000 hysteresis loop instrument. Figure 6 shows that the remanence of the samples increases slowly as accelerated corrosion time increases in the initial 24 h, and then, it decreases in the following corrosion process. The intrinsic coercivity has a significant decline for both samples over the initial 12 h corrosion period, then the reduction rate slows.

Intergranular corrosion mainly occurs in the initial stages, and the oxides are formed by combined ionization of rare earth elements, Fe element with water and oxygen. The oxides adhere to the magnets, which increases the remanence of the samples [21]. When accelerated corrosion time reaches 48 h, the remanence of SM samples is

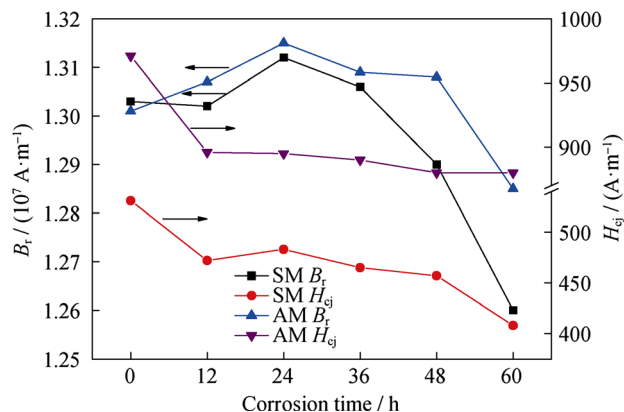


Fig. 6 Magnetic parameters of SM and AM samples after corrosion

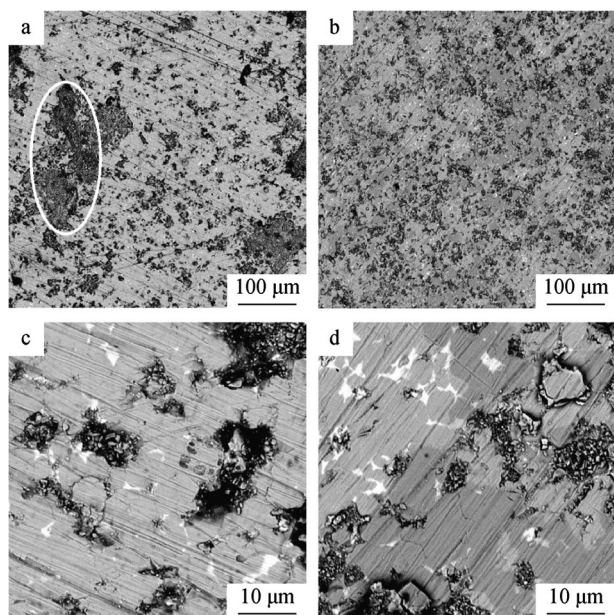


Fig. 7 BSE images for corrosion morphology of **a, c** SM and **b, d** AM samples with accelerated corrosion time for 60 h

significantly reduced, which is consistent with the mass loss. The coercivity of both samples reduces with the corrosion time, and the reducing rate becomes slower. The reduction in coercivity is caused by the corrosion of intercrystalline phase which acts as demagnetization coupling.

Besides, the corrosion morphology of samples with accelerated corrosion time of 60 h is observed after gently brushing samples surface by 2000-grit sandpaper. The black region in Fig. 7 refers to corrosion loss region of samples. The area of black region of SM samples is larger than that of AM samples, particularly the position marked by the white circle. The magnified images (Fig. 7c, d) show that corrosion depth of single corrosion area of SM samples is obviously deeper than that of AM samples. The deeper and larger corrosion areas of SM samples show more serious pitting and easier propagation of pitting.

4 Conclusion

The corrosion behavior of as-sintered and as-annealed $(\text{Nd}_{0.8}\text{Ce}_{0.2})_2\text{Fe}_{14}\text{B}$ magnets was studied. The mass loss of SM is larger than that of AM after accelerated corrosion tests. The free corrosion current of SM is larger than that of AM in $0.1 \text{ mol}\cdot\text{L}^{-1}$ HCl, but is smaller than that of AM in 3.5 wt% NaCl. The reason is that the annealing process reduces electrochemical activity of RE-rich phase and the electron transfer resistance which play the key role, respectively, in different aqueous solutions.

The inductance of Nyquist diagrams for SM in 3.5 wt% NaCl in the low-frequency region indicates that the pitting occurs in SM magnets. The deeper and larger corrosion areas of SM show more serious pitting and easier propagation of pitting. So the mass loss of SM has an obvious increase when the corrosion time is up to 48 h.

Acknowledgements This study was financially supported by the National Natural Science Foundation of China (No. 51571064) and the National Basic Research Program of China (No. 2014CB643701).

References

- [1] Sagawa M, Fujimura S, Togawa N, Matsuura Y. New material for permanent magnets on a base of Nd and Fe. *J Appl Phys*. 1984;55(6):2083.
- [2] Gutfleisch O, Willard MA, Brück E, Chen CH, Sankar SG, Liu JP. Magnetic materials and devices for the 21st century: stronger, lighter, and more energy efficient. *Adv Mater*. 2011;23(7):821.
- [3] Kaneko Y, Kuniyoshi F, Ishigaki N. Proven technologies on high performance NdFeB sintered magnets. *J Alloys Compd*. 2006;408–412:1344.
- [4] Watanabe N, Itakura M, Kuwano N, Li D, Suzuki S, Machida K. Microstructure analysis of sintered Nd–Fe–B magnets improved by Tb-vapor sorption. *Mater Trans*. 2007;48(5):915.
- [5] Bae KH, Kim TH, Lee SR, Namkung S, Jang T. Effects of DyH_x and Dy_2O_3 powder addition on magnetic and microstructural properties of Nd–Fe–B sintered magnets. *J Appl Phys*. 2012; 112(9):093912.
- [6] Liu Z, Davies HA. Elevated temperature study of nanocrystalline (Nd/Pr)–Fe–B hard magnetic alloys with Co and Dy additions. *J Magn Magn Mater*. 2005;290–291(2):1230.
- [7] Kim JY, Kwon HW, Lee JG, Yu JH. Decomposition of DyF_3 and its effect on magnetic performance of DyF_3 -doped Nd–Fe–B-type hot-deformed magnet. *J Appl Phys*. 2015; 117(17B):505.
- [8] Zhu MG, Li W, Wang JD, Zheng LY, Li YF, Zhang K, Feng HB, Liu T. Influence of Ce content on the rectangularity of demagnetization curves and magnetic properties of Re-Fe-B magnets sintered by double main phase alloy method. *IEEE Trans Magn*. 2014;50(1):1.
- [9] Zhu MG, Han R, Li W, Huang SL, Zheng DW, Song LW, Shi XN. An enhanced coercivity for (CeNdPr)–Fe–B sintered magnet prepared by structure design. *IEEE Trans Magn*. 2015; 51(11):1.
- [10] Hussain M, Zhao LZ, Zhang C, Jiao DL, Zhong XC, Liu ZW. Composition dependent magnetic properties of melt-spun La or/and Ce substituted nanocomposite NdFeB alloys. *Phys B*. 2016; 483:69.
- [11] Ni JJ, Ma TY, Yan M. Changes of microstructure and magnetic properties of Nd–Fe–B sintered magnets by doping Al–Cu. *J Magn Magn Mater*. 2011;323(21):2549.
- [12] Ni JJ, Zhou ST, Jia ZF, Wang CZ. Improvement of corrosion resistance in Nd–Fe–B sintered magnets by intergranular additions of Sn. *J Alloys Compd*. 2014;588(5):558.
- [13] Liu WQ, Yue M, Zhang DT, Zhang JX, Liu XB. Electrochemical corrosion behavior of Nd–Fe–B permanent magnets with modified microstructure. *J Appl Phys*. 2009;105(7):07A709.
- [14] Schultz L, ElAziz AM, Barkleit G, Mummert K. Corrosion behaviour of Nd–Fe–B permanent magnetic alloys. *Mater Sci Eng A*. 1999;267(2):307.

- [15] Barkleit G, ElAziz AM, Schneider F, Mummert K. Characterisation of electrochemical interactions between single phases of Nd–Fe–B permanent magnets. *Mater Corros.* 2001;52(3):193.
- [16] Viala F, Jolya F, Nevalainen E, Sagawac M, Hiragad K, Parkd KT. Improvement of coercivity of sintered NdFeB permanent magnets by heat treatment. *J Magn Magn Mater.* 2002; 242–245(2):1329.
- [17] Ni JJ, Zhang WW, Jia ZF, Wang CZ, Ma J. Effects of post-sinter annealing on the electrochemical corrosion resistance of Nd–Fe–B sintered magnets. *J Magn Magn Mater.* 2014;367:60.
- [18] Zhou SZ, Dong QF, Gao XX. *Sintered NdFeB–Rare Earth Permanent Magnet Materials and Technology.* Beijing: Metallurgical Industry Press; 2014. 134.
- [19] Zhang P, Ma TY, Liang L, Yan M. Improvement of corrosion resistance of Cu and Nb co-added Nd–Fe–B sintered magnets. *Mater Chem Phys.* 2014;147(3):982.
- [20] Huang SL, Feng HB, Zhu MG, Li AH, Li YF, Sun YC, Zhang Y, Li W. Optimal design of sintered $Ce_9Nd_{21}Fe_{bal}B_1$ magnets with a low-melting-point (Ce, Nd)-rich phase. *Int J Min Metall Mater.* 2015;22(4):417.
- [21] Wu YP, Zhu MG, Shi XN, Li W, Huang SL, Pan W. Corrosion research of $(Ce_{15}Nd_{85})_{30}Fe_{bal}B_1M$ sintered magnet in hydrothermal environment. *J Chin Soc Rare Earth.* 2016;34(2):171.
- [22] Yan G, McGuinness PJ, Farr JPG, Harris IR. Environmental degradation of NdFeB magnets. *J Alloy Compd.* 2009;478(1–2): 188.
- [23] Chen XB, Cain T, Scully JR, Birbilis N. Technical note: experimental survey of corrosion potentials for rare earth metals Ce, Er, Gd, La, and Nd as a function of pH and chloride concentration. *Corrosion.* 2014;70(4):323.
- [24] Li JJ. *Accelerated corrosion behavior of NdFeB permanent magnets in different corrosive climates.* Beijing: Central Iron & Steel Research Institute; 2012. 68.
- [25] Xu JL, Huang ZX, Luo JM, Zhong ZC. Corrosion behavior of sintered NdFeB magnets in different acidic solutions. *Rare Metal Mater Eng.* 2015;44(4):0786.
- [26] Gurappa I. Corrosion characteristics of permanent magnets in acidic environments. *J Alloys Compd.* 2003;360(1–2):236.
- [27] Song YW, Zhang H, Yang HX, Song ZL. A comparative study on the corrosion behavior of NdFeB magnets in different electrolyte solutions. *Mater Corros.* 2008;59(10):794.
- [28] Bala H, Pawlowska G, Szymura S, Rabinovich YM. Electrochemical corrosion characterisation of intermetallic phases occurring in Nd–Fe–B type magnets. *Br Corros J.* 1998;33(1): 37.
- [29] McCafferty E. *Introduction to Corrosion Science.* New York: Springer; 2009. 431.
- [30] Cao CN, Zhang JQ. *An Introduction to Electrochemical Impedance Spectroscopy.* Beijing: Science Press; 2002. 189.